

A Quick Startup Technique for High- Q Oscillators Using Precisely Timed Energy Injection

Hani Esmaealzadeh^{ID}, *Student Member, IEEE*, and Sudhakar Pamarti, *Member, IEEE*

Abstract—High-quality (Q) oscillators are notorious for being extremely slow during startup. Their long startup time increases the average power consumption in duty-cycled systems. This paper presents a novel precisely timed energy injection technique to speed up the startup behavior of high- Q oscillators. The proposed solution is also insensitive to the frequency variations of the injection signal over a wide enough range that makes it possible to employ an integrated oscillator to provide the injection signal. A theoretical analysis is carried out to calculate the optimal injection duration. As a proof-of-concept, the proposed technique is incorporated in the design of crystal oscillators and is realized in a TSMC 65-nm CMOS technology. To verify the robustness of our technique across resonator parameters and frequency variations, six crystal resonators from different manufacturers with different packagings and Q factors were tested. The implemented IC includes multiple crystal oscillators at 1.84, 10, and 50 MHz frequencies, with measured startup times of 58, 10, and 2 μ s, while consuming 6.7, 45.5, and 195 μ W at steady state, respectively. To the authors' best knowledge, this is the fastest, reported startup time in the literature, with $>15\times$ improvement over prior art, while requiring the smallest startup energy (~ 12 nJ).

Index Terms—Crystal oscillators, duty cycle, energy injection, Internet of Things, low power, microelectromechanical systems (MEMS), quality (Q) factor, startup time.

I. INTRODUCTION

AGGRESSIVELY duty-cycling the operation of electronic systems between ON and OFF states is an effective way of reducing the power consumption in ultra-low-power systems such as Internet-of-Things and biomedical implantable or wearable devices [1]–[5]. However, the rate of duty-cycling, and hence the amount of power saving, is constrained by the startup time of the system, which itself is limited by the long startup time of its reference oscillator. Crystal/MEMS resonators are commonly used as the reference oscillators in electronic systems. However, their extremely high quality factor ($Q \sim 100000$) makes them very slow during startup. For instance, a 10-MHz crystal oscillator, with reasonable power consumption, takes several milliseconds to turn ON and settle to within 10 ppm of its final frequency

Manuscript received July 21, 2017; revised September 8, 2017 and October 11, 2017; accepted October 19, 2017. This paper was approved by Guest Editor Rikky Muller. This work was supported by the National Science Foundation under Grant CNS-1329755. (Corresponding author: Hani Esmaealzadeh.)

The authors are with the Department of Electrical Engineering, University of California at Los Angeles, Los Angeles, CA 90095 USA (e-mail: haniaucla@ucla.edu).

Color versions of one or more of the figures in this paper are available online at <http://ieeexplore.ieee.org>.

Digital Object Identifier 10.1109/JSSC.2017.2766208

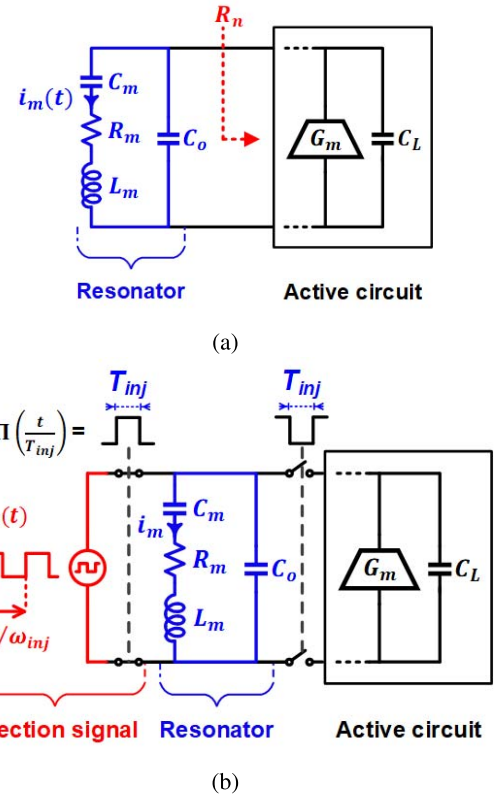


Fig. 1. (a) General form of an oscillator. (b) Startup time improvement through “pre-energization” of the resonator.

[6]–[11]. In contrast, the startup time of other circuit blocks such as low-dropout regulators and phase-locked loops is usually less than 10 μ s [12].

Consider the generic feedback oscillator shown in Fig. 1(a).¹ It has been shown (using a linear model [13]) that the startup time of an oscillator with an oscillation frequency of ω_{SS} , is

$$T_{\text{startup}} \propto \frac{Q}{\omega_{SS}} \cdot \left| \frac{1}{1 + R_n/R_m} \right| \cdot \ln \left(\frac{1}{i_m(0)} \right) \quad (1)$$

where R_m and R_n are the resonator's motional resistance and the negative resistance presented by the active circuitry, respectively, and $i_m(0)$ is the initial value of the current flowing into the motional branch of the resonator. It is evident that low-frequency, high- Q oscillators take a very long time to get started. Conventional enhanced startup techniques have mostly focused on increasing the magnitude of R_n in order to

¹Here, the resonator is modeled by its equivalent series RLC network, which is a valid model for most resonators such as crystals and MEMS.

quickly start the oscillator. This is done by either increasing the amplifier's transconductance [8], [14]–[16] or decreasing the capacitive loading of the resonator [17]–[19]. Nevertheless, both techniques achieve limited improvements. This is because the time constant only linearly scales with the transconductance and the amount of capacitor reduction is limited to the parasitic and stray capacitance of the printed circuit board. Besides, both techniques rely solely on amplifying circuit noise making the startup time sensitive to process, voltage, and temperature (PVT) variations—undesirable for precise duty-cycle control.

“Pre-energization” wherein a low- Q , integrated “injection” oscillator dumps a surge of energy into the resonator prior to the aforementioned feedback-based startup, as shown in Fig. 1(b), is emerging as an effective way to speed up a high- Q oscillator [20]–[22]. Since oscillation starts with a much bigger amplitude than circuit noise, it can potentially reach steady state in a shorter amount of time. The integrated “injection” oscillator, e.g., a ring or relaxation oscillator, itself starts up very quickly owing to its low Q factor. However, there are two major challenges associated with pre-energization: 1) there is usually a long transient time after the injection oscillator is disconnected and 2) startup time is very sensitive to the mismatch between the injection frequency, ω_{inj} , and the resonator's resonance frequency, ω_m . Since integrated ring and relaxation oscillators exhibit large sensitivity to PVT variations, researchers have resorted to calibration [21], [22], injection frequency chirping [16], or dithering [23] the injection frequency around the resonance frequency with limited success. These challenges of pre-energization is discussed in detail in Section II.

Esmaealzadeh and Pamarti [24] presented a technique that employs conventional single-frequency pre-energization, but only for a narrow, precisely controlled injection duration, $T_{inj,opt.}$. This technique reduced the startup time by $15\times$ compared to the best case in prior art. Furthermore, the achieved startup time is very predictable, and its sensitivity to ω_{inj} is reduced to the extent that simple, temperature-compensated integrated oscillators can be used as the injection signal.

This paper elaborates on [24], describing the technique and important circuit design aspects that reduce it to practice, especially over PVT corners. In addition, a new analysis that quantifies the technique's reduced sensitivity to the injection frequency mismatch and other circuit errors is described. Section III explains the main concept and an analysis of the “precisely timed energy injection” technique. Section IV quantifies the impacts of the injection frequency and duration errors on the startup time. Section V details the implemented circuit, and Section VI describes detailed measurement results from the prototype in [24].

II. PRE-ENERGIZATION: PREVIEW AND CHALLENGES

The simplified schematic shown in Fig. 1(b) is a general representation of pre-energization in prior art: the resonator is driven open loop by a voltage source, $v_s(t)$, for a finite but arbitrary duration, T_{inj} . In most cases, $v_s(t)$ is a square wave of frequency ω_{inj} .

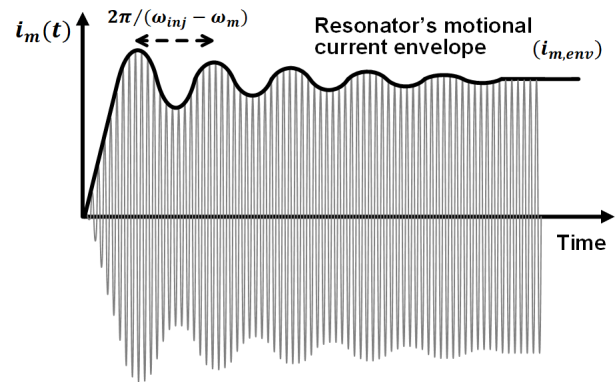


Fig. 2. Transient response of the motional current of a high- Q resonator driven by a square-wave/sinusoidal injection signal.

The transient response of a (second-order) high- Q resonator, when driven by a square- (or sine-) wave injection oscillator, is plotted in Fig. 2. So, during pre-energization, the envelope of the motional current, $i_{m,env}(t)$, follows an underdamped response and reaches $i_{m,env}(T_{inj})$ at the end of the injection period, i.e., at $t = T_{inj}$. Subsequently, the oscillator settles, slowly, starting from $i_{m,env}(T_{inj})$ till its steady-state value, $I_{m,ss}$, is reached, as illustrated in Fig. 3 for different values of T_{inj} .

This presents two significant problems. First, the startup time is minimized only if the energy deposited in the resonator during pre-energization is equal to the energy under steady-state oscillation, i.e., $i_{m,env}(T_{inj}) = I_{m,ss}$, as shown in Fig. 3(b). Otherwise, as is evident in Fig. 3(a), the oscillator will have a long transient settling upon disconnecting the injection signal to adjust the energy level. This slow transient settling results in a long startup time, thereby limiting the benefits of pre-energization. Furthermore, $i_{m,env}(T_{inj})$, and hence the settling time, can vary significantly over PVT corners.

Second, owing to the high Q of the resonator (typically 100 K–1 M), unless ω_{inj} is within about ± 500 ppm of ω_m , the resonator rejects much of the injected energy rendering the technique ineffective. As a result, the startup time is very sensitive to the frequency mismatch between the injection frequency, ω_{inj} , and the resonator's resonance frequency, ω_m . Calibration of the injection oscillator [21], [22] reduces static frequency mismatches, but even the best temperature-compensated integrated oscillators exhibit more than ± 5000 ppm frequency mismatch over PVT variations [25]–[30]. Injection frequency chirping [16] and dithering [23] around ω_m , as shown in Fig. 4, have been employed with the hope that ω_{inj} approaches ω_m at least for a small duration during the pre-energization period. However, the amount of energy dumped into the resonator at the end of the injection period is still very small resulting in a long and PVT-variant settling transient.

III. PRECISELY TIMED ENERGY INJECTION

A. Concept

The proposed technique is based on the fundamental realization that *the amount of energy injected into the resonator is*

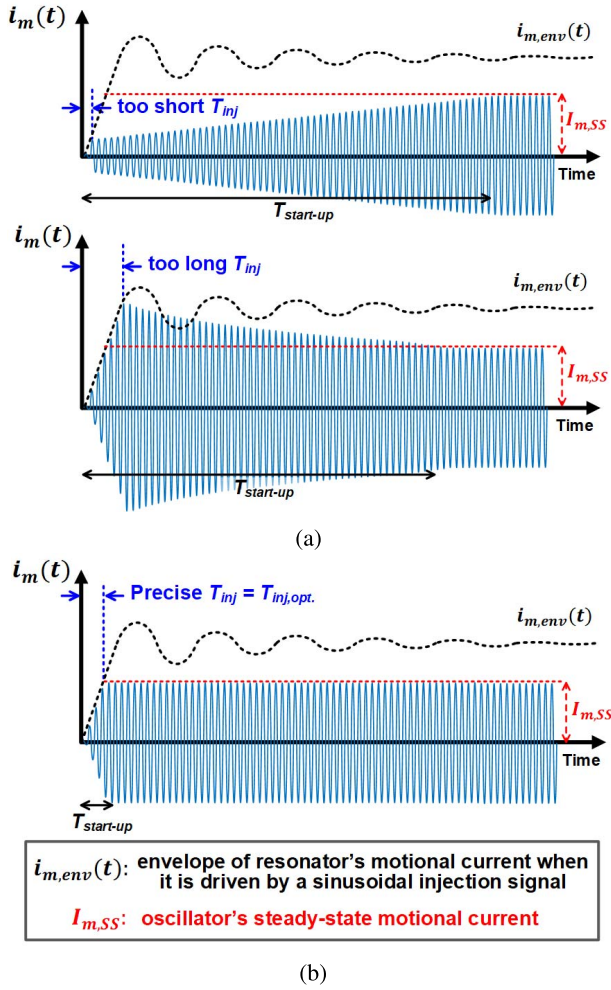


Fig. 3. Impact of injection duration on the startup time for three different cases of (a) short, long, and (b) optimum injection durations.

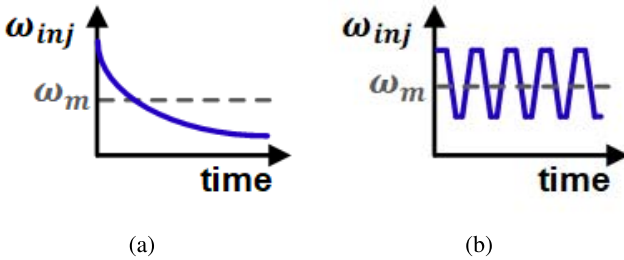


Fig. 4. Prior solutions to overcome the frequency mismatch problem. (a) Chirp injection. (b) Dithered injection.

determined not just by the injection frequency, ω_{inj} , but also, just as significantly, by the duration of injection, T_{inj} [24]. The technique simply terminates pre-energization precisely at the right time, $T_{inj} = T_{inj,opt.}$, such that the energy built up in the resonator is equal to its value under steady-state closed-loop oscillation condition, i.e., when $i_{m,env}(T_{inj,opt.}) = I_{m,SS}$. As shown in Fig. 3(b), ideally there will be no settling transient upon disengagement of the injection oscillator, thereby minimizing the startup time. Section III-B calculates the optimal injection duration, $T_{inj,opt.}$, while Section III-C describes a simple technique to make $T_{inj,opt.}$ a PVT-invariant constant that can be set without *a priori* knowledge of $I_{m,SS}$.

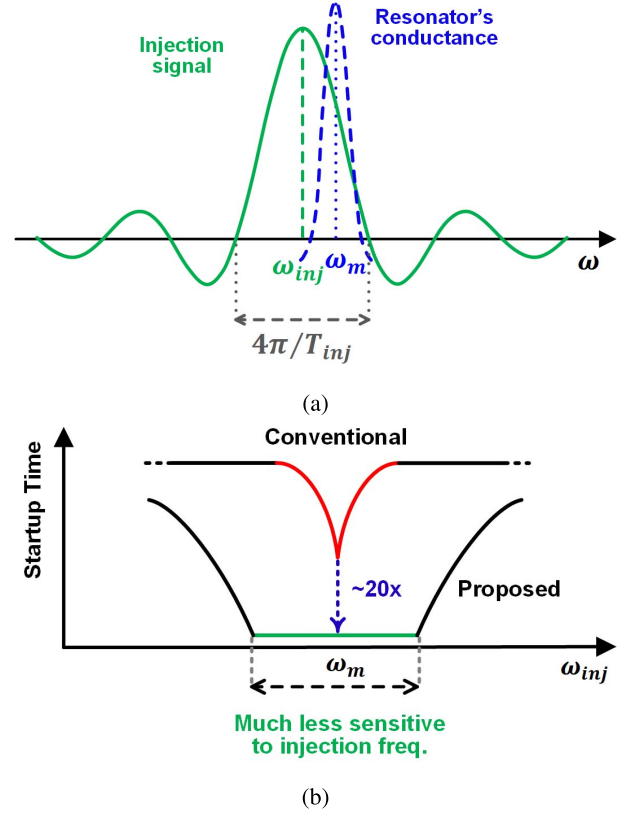


Fig. 5. Sensitivity of the proposed precisely timed energy injection to the variations in the injection frequency. (a) In frequency domain, the injection signal is a relatively wideband sinc function. (b) Startup time of the proposed solution is much less sensitive to the frequency mismatch as opposed to the conventional case.

It is important to note that the optimal injection duration, $T_{inj,opt.}$, marks the first time when the motional current's envelope reaches the target value, $I_{m,SS}$, during pre-energization. As shown later, this makes the startup time a very small value, e.g., just ~ 100 number of cycles for the different measured cases in the demonstrated prototype (see Section VI). More importantly, note that single-frequency pre-energization for such a short duration, $T_{inj,opt.}$, amounts to driving the narrow-band resonator in open loop with a very wide bandwidth sinc-shaped² signal centered at ω_{inj} , with a main lobe width of $4\pi/T_{inj}$, as shown in Fig. 5(a). The wide main lobe ensures that the resonator is sufficiently energized even for a large mismatch between ω_{inj} and ω_m , unlike conventional pre-energization. Consequently, the proposed quick startup technique is much less sensitive to the injection frequency errors than prior art, as depicted in Fig. 5(b). Section IV provides a quantitative analysis of this effect. It is important to note that in the case of conventional pre-energization (arbitrary T_{inj}), even with perfectly matched injection and resonance frequencies, the oscillator still might take a long time to get started due to under/over energization of the resonator as shown in Fig. 3(a). This explains the lower startup time of the proposed solution compared with the conventional technique in Fig. 5(b).

Another by-product of using a small injection duration is the low startup energy consumption as all the startup auxiliary

²Here, a sinc function is defined as $\text{sinc}(x) = \sin(x)/x$.

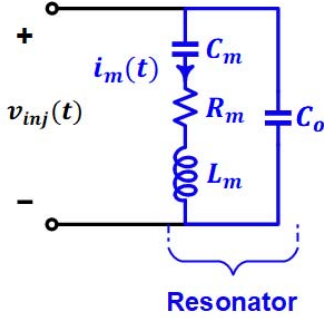


Fig. 6. Resonator driven by an arbitrary injection signal.

circuitry is ON only for the short duration of $T_{inj,opt.}$. This is verified by our measurement results in Section VI.

In summary, as shown in Figs. 3(b) and 5(b), precisely timing the injection duration addresses both of the challenges in pre-energization, namely, *sensitivity to injection frequency* and *long transient time*. The rest of this paper provides an analysis to compute the optimal injection duration and how to make it invariant over PVT variations.

B. Injection Duration (T_{inj})

As Fig. 3(b) suggests, startup time is minimized when

$$i_{m,env}(t = T_{inj,opt.}) = I_{m,SS}. \quad (2)$$

To determine $i_{m,env}(t)$, consider a high- Q resonator driven by an arbitrary voltage source, $v_{inj}(t)$ as shown in Fig. 6. As derived in the Appendix, the envelope of the motional current is given by

$$i_{m,env}(t) = |V_{inj+}(j\omega_m)| \cdot \frac{e^{-\frac{t}{\tau}}}{L_m} \quad (3)$$

where $V_{inj+}(j\omega) = V_{inj}(j\omega)$ for $\omega > 0$, but 0 otherwise, i.e., it is the positive-frequency half of the Fourier transform of $v_{inj}(t)$, and $\tau = 2Q/\omega_m$ is the time constant of the circuit.

In case of the finite injection shown in Fig. 1(b), it can be shown that during pre-energization, i.e., $0 \leq t \leq T_{inj}$, $v_{inj}(t) = v_S(t) \cdot \Pi(t/T_{inj})$, where $\Pi(t)$ is a unit pulse of unit time duration. As a result, for the case of injecting a single frequency,³ i.e., $v_S(t) = V_{inj} \cdot \cos(\omega_{inj}t)$, $V_{inj+}(j\omega)$ is simply a sinc function translated in frequency to ω_{inj} . Hence, using (3), it can be shown that the envelope of the motional current at the end of the injection duration, T_{inj} , is

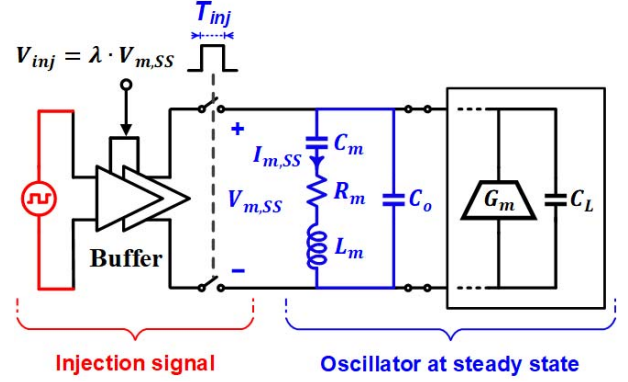
$$i_{m,env}(T_{inj}) = \frac{T_{inj} \cdot V_{inj}}{2L_m} \cdot \left| \text{sinc} \left[\frac{T_{inj}}{2} \cdot \Delta\omega_{inj} \right] \right| \cdot e^{-\frac{T_{inj}}{\tau}} \quad (4)$$

where $\Delta\omega_{inj} = \omega_{inj} - \omega_m$ is the mismatch between the injection and resonance frequencies.

Assuming $T_{inj} \ll \tau$ and $T_{inj} \cdot |\Delta\omega_{inj}| \ll 2$, the optimum injection duration can be shown to be

$$T_{inj,opt.} = \frac{2L_m \cdot I_{m,SS}}{V_{inj}}. \quad (5)$$

³Due to the high Q factor of the resonator, considering only the first harmonic of a square-wave driving source is sufficient, where $V_{inj} = (4/\pi) \cdot V_d$, and V_d is the square-wave amplitude.

Fig. 7. Constant, PVT-insensitive injection duration by making the injection amplitude (V_{inj}) track the steady-state oscillation amplitude ($V_{m,SS}$).

C. PVT-Invariant Injection Duration

Although it is conceptually simple, realizing $T_{inj,opt.}$ in practice is problematic since $I_{m,SS}$ and V_{inj} vary over PVT, and L_m depends on the resonator's process variations. Our solution is to make V_{inj} track the steady-state amplitude across the resonator under normal oscillation conditions, $V_{m,SS}$, as illustrated in Fig. 7. By making $V_{inj} = \lambda \cdot V_{m,SS}$, where λ is a suitable constant, and noting that the ratio $I_{m,SS}/V_{m,SS}$ is the resonator's motional admittance, $T_{inj,opt.}$ reduces to

$$T_{inj,opt.} = \frac{1}{\lambda \cdot \Delta\omega_{SS}}. \quad (6)$$

Note that the chosen constant λ can be precisely implemented using a feedback amplifier. Note also that $\Delta\omega_{SS} = \omega_{SS} - \omega_m$ is the difference between the steady-state oscillation frequency, ω_{SS} , and the resonator's resonance frequency, ω_m , and it too has minimal variations thanks to the high stability of high- Q reference oscillators such as crystal and/or MEMS oscillators. Therefore, according to (6), $T_{inj,opt.}$ is a very predictable and constant number that can be calculated and set at design time.

It is important to note that the steady-state oscillation amplitude, $V_{m,SS}$, is not usually known before the oscillator has started up. Furthermore, $V_{m,SS}$ can vary over PVT corners. Hence, the implementation of the technique shown in Fig. 7 requires delicate consideration. For instance, in oscillators that peg $V_{m,SS}$ to a fixed reference (bandgap) voltage, V_{ref} , by using an amplitude regulator, then V_{inj} can be simply set using V_{ref} . In this paper, we consider the popular case of the Pierce oscillator with an amplitude regulator proposed in [31], which provides a $V_{m,SS}$ that linearly varies over temperature. Therefore, as described in Section V-A, a proportional to absolute temperature (PTAT) regulator can be used to set the injection amplitude, V_{inj} .

IV. IMPACT OF INJECTION FREQUENCY AND DURATION ERRORS ON STARTUP TIME

This section quantifies the impact of injection frequency and timing errors on the startup time, i.e., the impact of nonzero values of $\Delta\omega_{inj} = \omega_{inj} - \omega_m$ and $\Delta T_{inj} = T_{inj} - T_{inj,opt.}$.

Startup time is generally defined as the time required to first reach and subsequently stay within a target frequency

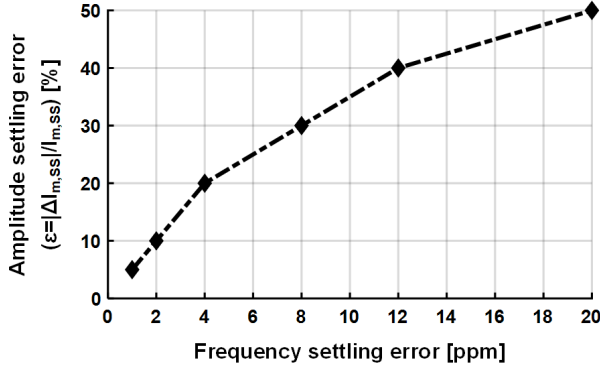


Fig. 8. Simulation result of amplitude settling error versus frequency settling error for a 50-MHz crystal oscillator.

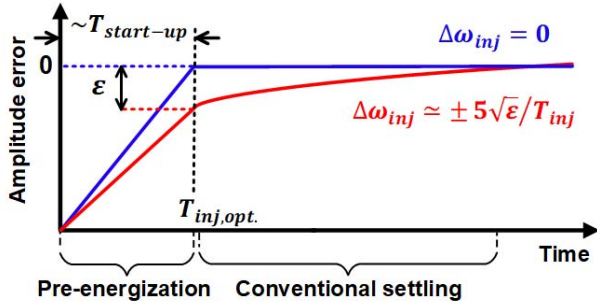


Fig. 9. Impact of $\Delta\omega_{inj} = \omega_{inj} - \omega_m$ on amplitude settling.

settling error. Since measuring real-time frequency with part per million accuracy, especially for very low startup times, is very challenging, we quantify the startup time in terms of a target oscillation amplitude settling error, ε .

Note that using amplitude settling behavior as a proxy for frequency settling behavior is a common practice [16], [32]. To independently verify, we have performed thorough transistor-level circuit simulations of a typical 50-MHz crystal oscillator without and with the proposed fast startup technique. Fig. 8 shows the simulated relationship between the amplitude and frequency settling errors for the fast startup technique. The monotonic relation clearly suggests that amplitude settling is a valid proxy for frequency settling measurements. For instance, the frequency error at 90% amplitude ($\varepsilon = 10\%$) is within 2 ppm, which explains why in prior art (see [16], [32]) the startup time is often measured as the time at which the oscillation amplitude is at 90% of its steady-state value.

Now, the effect of $\Delta\omega_{inj}$ and ΔT_{inj} on the startup time can be quantified in terms of a target amplitude settling error, ε , and Fig. 8 can translate it to an equivalent target frequency settling error.

Fig. 9 depicts typical amplitude settling in the proposed fast startup technique. Ideally, when there are no frequency or timing errors, i.e., $\Delta\omega_{inj} = 0$ and $\Delta T_{inj} = 0$, then the motional current amplitude at the end of the pre-energization period is exactly equal to its value under steady-state oscillations, i.e., there is no subsequent transient and the startup time is exactly $T_{startup} = T_{inj,opt}$.

However, any errors will result in an amplitude error, ε , at the end of the pre-energization period, as illustrated for the

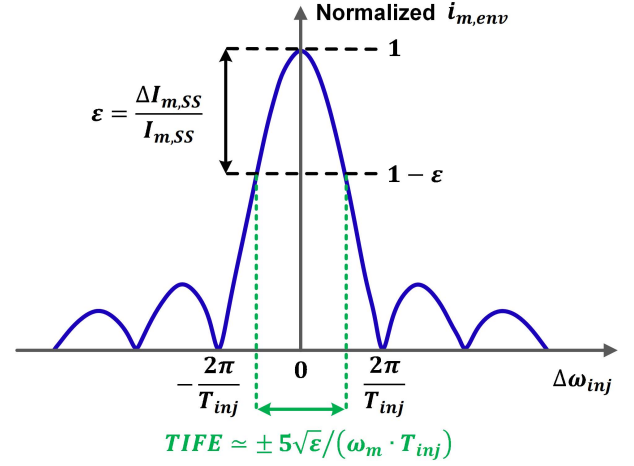


Fig. 10. Variations in $I_{m,ss}$ as a function of frequency mismatch, $\Delta\omega_{inj} = \omega_{inj} - \omega_m$. In order to maintain an ε variation in $I_{m,ss}$, the frequency mismatch needs to be kept within $\pm 5\sqrt{\varepsilon}/T_{inj}$.

case of $\Delta\omega_{inj} \neq 0$ in the figure. Conventional oscillator settling will subsequently reduce the motional current amplitude (and frequency) errors from ε toward zero. However, a startup time of $T_{inj,opt}$ is guaranteed simply by ensuring that the total motional current amplitude settling error at the end of the pre-energization period is smaller than the target ε .

A. Tolerable Injection Frequency Error

The dependence of the motional current's envelope value at the end of the pre-energization period, $i_{m,env}(T_{inj})$, on the injection frequency error, $\Delta\omega_{inj}$, was already derived in Section III-B, specifically in (4). This dependence is plotted in Fig. 10. Note that it simply follows the sinc-function shape of the Fourier transform of the injection signal. It can be shown that the normalized motional current amplitude error is less than ε if

$$|\Delta\omega_{inj}| \leq \frac{5\sqrt{\varepsilon}}{T_{inj,opt}} \quad (7)$$

as shown in the figure. Normalized to ω_m , this represents the tolerable injection frequency error (TIFE) for which the startup time needed to reach a target amplitude settling error, ε , remains $T_{startup} = T_{inj,opt}$.

$$\text{TIFE}(\varepsilon) = \frac{\Delta\omega_{inj}}{\omega_m} \cong \pm 5\sqrt{\varepsilon} \cdot \lambda \cdot p \quad (8)$$

where $p = (\omega_{ss} - \omega_m)/\omega_m$ is the frequency pulling factor of the high- Q oscillator.

Fig. 11 plots the calculated TIFE as a function of both the amplitude and frequency settling errors for $\lambda = 2$ and $p = 2000$ ppm, where Fig. 8 was used to translate from amplitude to frequency settling errors. As can be seen, the startup time to reach within 2 ppm of frequency error (i.e., for $\varepsilon = 10\%$), remains invariant over TIFE of ± 6300 ppm, which agrees with the measured TIFE in Section VI. State-of-the-art, temperature-compensated, integrated oscillators [25]–[30] have temperature sensitivities well within this range, which guarantees that they can be used for successful quick startup

[illegible]

over the required operating temperature range, as described later in Section V.

It is interesting to examine the dependence of TIFE on the Q factor of the resonator. A theoretical study in [33] has shown that the pulling factor, p , has the following dependence on the Q factor:

$$\frac{dp}{dQ} = \frac{-1}{2Q^2} \cdot \frac{1}{\sqrt{\left(\frac{R_n}{R_m}\right)^2 - 1}}. \quad (9)$$

As seen in (9), for a high- Q oscillator, (dp/dQ) is negligible suggesting that the pulling factor, and hence the TIFE, are almost independent of the Q factor.

It is worth noting that the improved TIFE of this paper is a result of using a precise, short T_{inj} . Even though the key idea of precisely timed injection is applied to the case of a single-frequency $v_S(t)$ in this paper, the same idea can be combined with frequency chirping and/or frequency dithering to improve the TIFE of these techniques. The calculation of $T_{\text{inj,opt.}}$ for frequency chirping/dithering is beyond the scope of this paper, however, one can follow the same procedure outlined in Section III-B to determine the ideal $T_{\text{inj,opt.}}$ in each of these cases.

B. Tolerable Injection Duration Error

The actual injection duration, T_{inj} , can deviate from the ideal value, $T_{\text{inj,opt.}}$, for various reasons. The duration error, ΔT_{inj} , will result in an error in the motional current amplitude at the end of pre-energization. For small values of T_{inj} , $I_{m,\text{ss}}$ linearly tracks T_{inj} , as is evident from both Fig. 2 and (4). Consequently, the normalized amplitude error remains less than ε , if $|\Delta T_{\text{inj}}| < \varepsilon \cdot T_{\text{inj}}$. This represents the tolerable injection duration error (TIDE). For instance, as shown by the measurement results (see Section VI), for the case of $\varepsilon = 10\%$, the startup time remains constant for $\pm 10\%$ variations in T_{inj} .

V. CIRCUIT IMPLEMENTATION

The block diagram of the proposed precisely timed energy injection technique incorporated in a crystal oscillator is shown

in Fig. 12. The crystal oscillator is implemented in a commonly used Pierce configuration along with an amplitude regulator loop [31], [34], [35]. A PTAT voltage regulator is used to set the injection amplitude, V_{inj} , during startup. As explained in the following section, a PTAT source makes V_{inj} linearly track $V_{m,\text{SS}}$ over temperature fluctuations in order to guarantee a constant $T_{\text{inj,opt.}}$. Since our proposed technique relaxes the matching requirement between ω_{inj} and ω_m , a simple temperature-compensated ring oscillator with a temperature sensitivity of 85 ppm/ $^{\circ}\text{C}$ is used as the injection oscillator. At startup, switch S_1 connects the injection (ring) oscillator to the crystal resonator, through a buffer, for the fixed duration of $T_{\text{inj,opt.}}$, during which $i_{m,\text{env}}$ builds up to its steady-state value, $I_{m,\text{SS}}$.

A simple timer is used to control $T_{\text{inj, opt.}}$ by counting an appropriate number ($N = 1/2\pi\lambda p$) of full cycles of the ring oscillator. Note that λ and p , and hence the number of cycles, N , is known *a priori*. As shown in our measurements in Section VI, the number of cycles, N , is ~ 100 . Since we are counting the cycles of the ring oscillator, the timing error, $|\Delta T_{\text{inj}}|$, is less than 0.5 cycle corresponding to only 0.5% error, which is well within the required TIDE of $\pm 10\%$. As shown in Fig. 12, the injection signal and the timer's clock are derived from two different phases of the ring oscillator (R_{0° and R_{90°). This ensures that the amplitude regulator is not interrupted with any abrupt voltage change at the end of $T_{\text{inj, opt.}}$, and hence, it performs a smooth and fast settling. Switches S_2 and S_3 are also used to isolate the amplitude regulator from the fluctuations in the injection signal. Even though a single-ended injection is shown in Fig. 12 for the sake of simplicity, the actual implementation is done differentially. To save power, all the startup auxiliary circuitry is turned OFF at the end of $T_{\text{inj, opt.}}$, which leads to a low-startup energy consumption. The following sections go over the design of the main crystal oscillator, the injection oscillator, and the buffer in more detail.

A. Crystal Oscillator With Amplitude Regulator Loop

Amplitude regulators are prevalently used in crystal oscillators to control the oscillation amplitude, $V_{m,SS}$. By adaptively adjusting the bias current, amplitude regulators

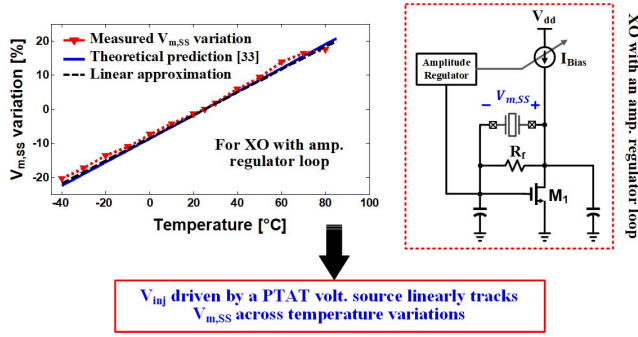


Fig. 13. Steady-state oscillation amplitude, $V_{m,SS}$, of a crystal oscillator with an amplitude regulator loop linearly varies over temperature.

decrease the contribution of the active circuit's nonlinearities toward the oscillation amplitude and frequency [31]. Therefore, a more stable and predictable oscillation amplitude/frequency is obtained over PVT variations.

Analysis in [33] shows that the oscillation amplitude of a crystal oscillator with an amplitude regulator loop linearly varies over temperature. As it is evident from Fig. 13, the measured variations of $V_{m,SS}$ linearly change over temperature, which agrees with the theoretical prediction. As a result, if V_{inj} is set by a PTAT voltage regulator, as shown in Fig. 12, it would linearly track the variations in $V_{m,SS}$. Consequently, $T_{inj,opt.}$ becomes a PVT-invariant constant, following the analysis carried out in Section III-C. Note that since $\pm 10\%$ variations in $T_{inj,opt.}$ is tolerable, the linear approximation in Fig. 13 needs to be only $\pm 10\%$ accurate. Note that, in practice, in order to determine the value of λ , the value of $V_{m,SS}$ is needed to be known at one arbitrary temperature.

B. Temperature-Compensated Ring Oscillator

According to the discussion in Section III-A and the analysis in Section IV-A, the proposed technique is very tolerant of large frequency mismatch between ω_{inj} and ω_m . As long as the frequency mismatch is within the TIFE given by (8), the transient after T_{inj} , and hence the startup time, is minimized. This enables the use of a simple on-chip ring oscillator as the injection signal. The ring oscillator is designed using the simple temperature-compensation technique proposed in [25]. The schematic of the ring oscillator is shown in Fig. 14(a), where a low-variation current source is used to bias the ring oscillator. The analysis in [25] and [36] is used to obtain the optimized design parameters to ensure a stable bias current I_b —the sum of I_1 and I_2 —and hence, a stable oscillation frequency in the presence of temperature fluctuations.

In order to compensate for the variations in CMOS fabrication process, the sizes of the transistors in Fig. 14(a), and hence the value of the bias current I_b , are initially trimmed by using proper static control bits. Fig. 14(b) shows the measured sensitivity of the ring oscillator's frequency to the temperature variations. On-chip oscillators with lower temperature sensitivities have been reported [28]–[30], however, the sensitivity shown in Fig. 14(b) is sufficient for successful quick startup over the industrial temperature range, as verified by our measurement results in Section VI.

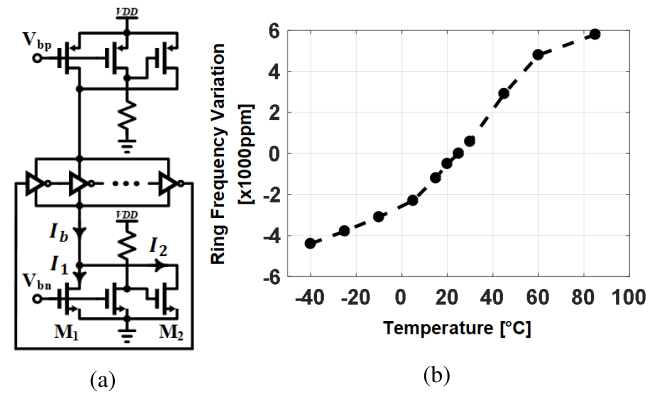


Fig. 14. Temperature-compensated, current-starved ring oscillator [25]. (a) Schematic and (b) measured variation of oscillation frequency over temperature.

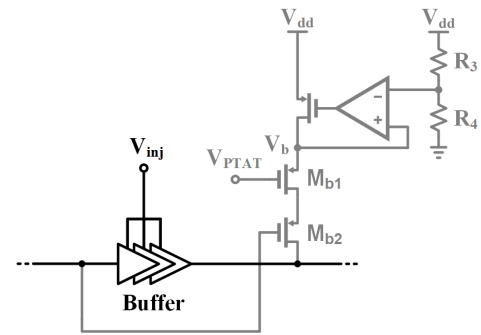


Fig. 15. Simple technique to reduce the output slew-rate variation of the buffer under temperature variations.

C. Buffer

The buffer between the ring oscillator and the resonator in Fig. 12 is employed to drive the resonator and isolate the ring oscillator from the large capacitive load ($2C_L > 13$ pF). The buffer is made up of a chain of standard tapered inverters [37]. Note that since the supply voltage of the buffer (V_{inj}) varies in a PTAT manner, the slope (slew rate), and hence the fundamental frequency component of the injection signal varies over temperature. According to the analysis in Section IV, also verified by the measurement results in Section VI, for $\varepsilon = 10\%$, variations within $\pm 10\%$ would not cause any significant degradation in the startup time. However, as shown in Fig. 15, transistors M_{b1} and M_{b2} , along with a voltage regulator, are added to adjust the pull-up strength of the buffer in case V_{PTAT} changes considerably at hot/cold temperatures. Note that as long as V_b in Fig. 15 is lower than V_{inj} , the output level of the buffer is set by V_{inj} with proper slew-rate control. Furthermore, using an inverter chain sharpens the transitions in the injection signal and decreases their variations over PVT.

VI. MEASUREMENT RESULTS AND COMPARISON

A prototype IC was fabricated in a TSMC 65-nm standard CMOS process [24]. The test board along with the die micrograph is shown in Fig. 16. The IC includes three different crystal oscillators, targeting 1.843, 10, and 50 MHz. To verify the

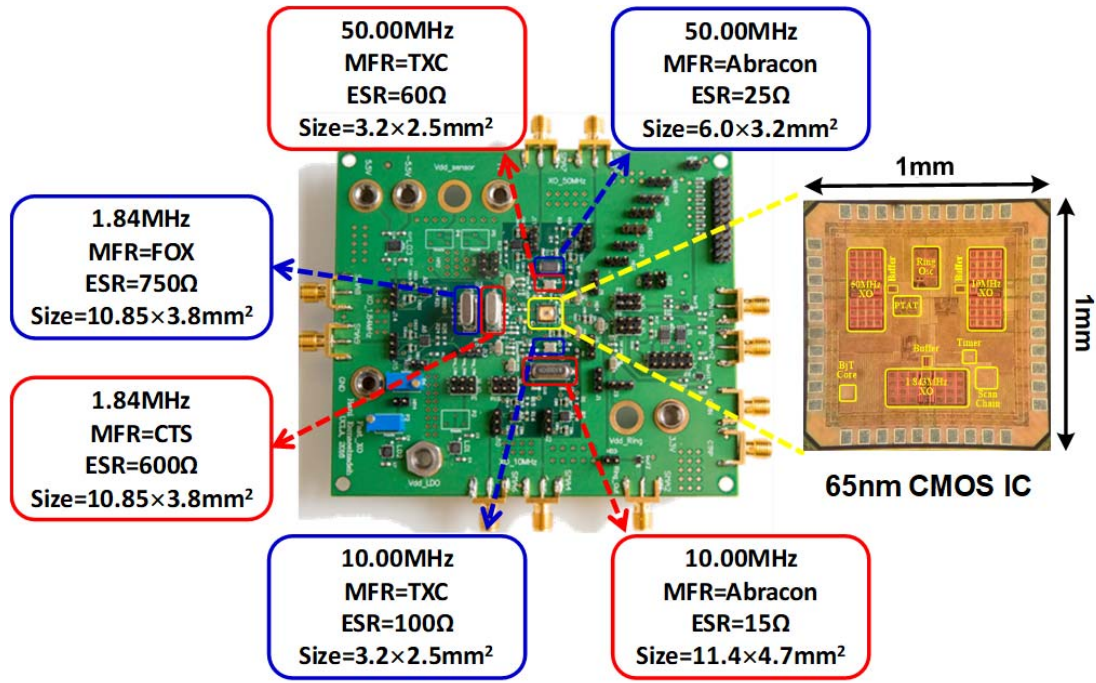


Fig. 16. Implemented test board including the fabricated IC and six different tested crystal devices.

TABLE I
ENERGY CONSUMPTION BREAKDOWN DURING STARTUP

Frequency (MHz)	Start-up energy (nJ)		
	1.84	10.0	50.0
Buffer	6.25	10.1	8.74
Ring oscillator	0.75	0.9	0.5
PTAT regulator	4.5	0.9	0.1
Digital circuitry (timer)	0.1	0.1	0.06
Total start-up energy (nJ)	11.6	12	9.4

robustness of the proposed technique over crystal parameters and frequency variations, two crystal devices with different packagings and Q factors from different manufacturers were tested for each oscillator, as shown in Fig. 16. The active area is 0.09 mm^2 per crystal oscillator in a $1 \text{ mm} \times 1 \text{ mm}$ die. Most of the active area is occupied by the MIM capacitor banks, included for debug/testing purposes. Note that a bipolar junction transistor core is used to measure the Si temperature, but only because it facilitates testing the IC over the industrial temperature range.

Fig. 17 shows the measured transient output voltage of the 10-MHz oscillator for three different injection durations. The output voltage is measured at the gate of the transistor M_1 in Fig. 12. In order to isolate the oscillator from the input impedance of the measuring probe, an off-the-shelf discrete operational amplifier (ADA4817) in a unity-gain feedback configuration is used to act as a high-speed analog buffer

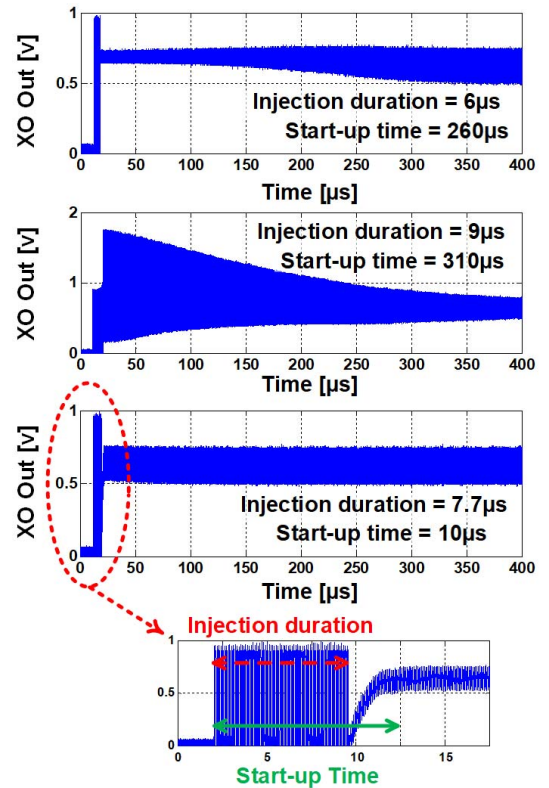


Fig. 17. Measured transient response of the 10-MHz oscillator during startup (measured at the gate of M_1 in Fig. 12) for three different injection durations: startup time is minimized for $T_{inj,opt.} = 7.7 \mu\text{s}$.

between the oscillator and the probe. As is evident in Fig. 17, there is a long transient time after injection, if the injection duration is not equal to its optimum value of $7.7 \mu\text{s}$, calculated from (6). However, the output signal quickly reaches

TABLE II
PERFORMANCE SUMMARY AND COMPARISON WITH PRIOR ART

	RFIC'09 [8]	TI-CC2650 [22]	JSSC'16 [16]	ISSCC'16 [23]	ISSCC'17 [19]	This work [24]					
CMOS process (nm)	130	N/A	180	65	90	65					
Supply voltage (V)	1.2	3.0	1.5	1.68	1.0	1.0					
Active area (mm ²)	N/A	N/A	0.12	0.08	0.072	0.09 per XO					
Frequency (MHz)	19	24	39	24	24	50	10	1.8432			
Xtal manufacturer	N/A	N/A	Daishinku	N/A	N/A	Abracon	TXC	Abracon	TXC	CTS	FOX
Load capacitance (pF)	N/A	N/A	8	6	10	9	9	9	8	6.5	6.5
Steady-state power consumption (μ W)	27	N/A	181	393	95	74.2	195	23.6	45.5	6.7	8.6
Start-up energy (nJ)	N/A	N/A	349	N/A	36.7	9.4	13.3	13.5	12	11.6	12.7
Start-up time* (μ s)	1200	150	158	64	200	1.95	2.2	11.3	10	58	64
Start-up time (No. of cycles)	22800	3600	6162	1536	4800	98	110	113	100	107	118
Start-up variation over temperature	N/A	N/A	$\pm 7\%$ (-30 to 125°C)	$\pm 35\%$ (-40 to 90°C)	27.5% (-40 to 90°C)	10%	7%	5%	3%	9%	8%
Technique	High g_m	Calibrated RC-Osc. injection	Chirp injection + negative resistance boost	Dithered injection	Dynamically-adjusted load	Precisely-timed injection					

*Start-up time is defined as the time it takes for the oscillation amplitude to reach 90% of its steady-state value (same definition as prior art).

steady state when the right amount of $T_{inj,opt.} = 7.7 \mu s$ is applied. This result corroborates the proposed theory presented in Section III.

To demonstrate the resilience of the proposed technique, intentional errors in the injection duration, T_{inj} , and the injection frequency, ω_{inj} , are introduced, and the measured startup times are plotted in Fig. 18(a) and (b), respectively, for the 10-MHz oscillator. There is no noticeable degradation in the startup time for up to $\pm 10\%$ variation in $T_{inj,opt.}$, and up to ± 6500 ppm mismatch between ω_{inj} and ω_m . For comparison's sake, Fig. 18(b) also plots the measured startup time for conventional pre-energization, i.e., when $T_{inj} \neq T_{inj,opt.}$, but an arbitrary $T_{inj} = 6 \mu s$ is used instead. As can be seen in Fig. 18(b), the proposed technique demonstrates $20\times$ lower startup time and dramatically lower sensitivity to the injection frequency as well.

It is important that the power overhead needed for the fast startup circuitry be minimized in order to reduce the overall energy consumption. Table I shows the breakdown of the startup energy consumed by each of the startup auxiliary circuitry. As can be seen, the largest contributor to energy consumption is the buffer mainly because it has to drive the crystal's large capacitive load. To the authors' best knowledge, the proposed technique in this paper has the lowest startup energy in the literature (see Table II). The low-startup energy of this paper is a direct result of having a small injection duration.

Fig. 19 shows the measured startup time variations over temperature for each of the six tested crystal oscillators. The injection duration for each case, $T_{inj,opt.}$, is calculated from (6). The worst case startup time variation is within 10%.

Table II summarizes the measured performance of the proposed precisely timed energy injection technique, and compares the results with other fast startup techniques reported

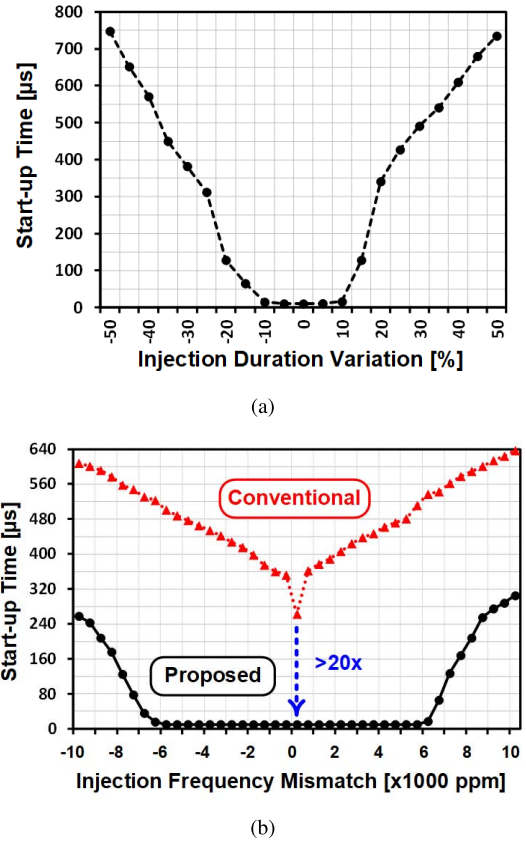


Fig. 18. Measured startup sensitivity of the 10-MHz oscillator. (a) Sensitivity to the variations in the optimal injection duration. (b) Sensitivity to the injection frequency mismatch: proposed technique shows more than $20\times$ faster startup with much less sensitivity to the injection frequency.

in the literature. Since startup time scales with the oscillation frequency, to normalize over frequency, the number of cycles needed for startup is also reported for each design. As can

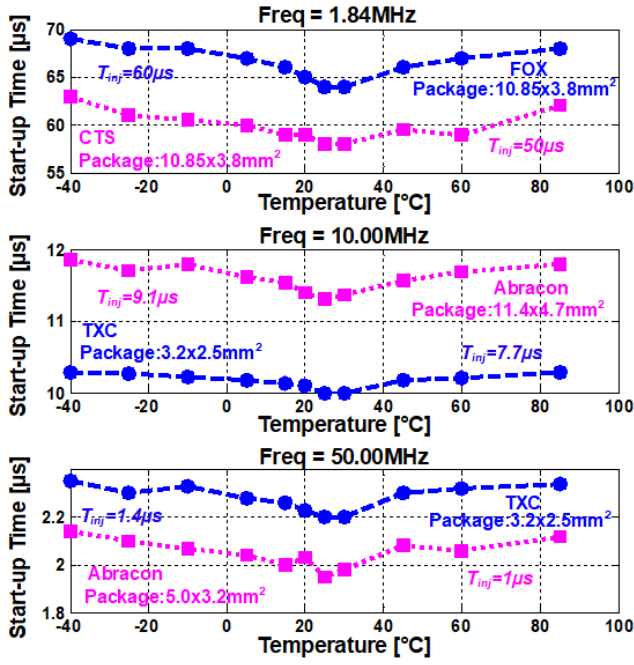


Fig. 19. Measured crystal oscillator startup variations over temperature for six different crystal devices (ESR ranging from 15 to 750 Ω) at three different frequencies.

be seen, employing the proposed solution, the crystal oscillator, in all the tested cases, only takes about 100–120 number of cycles to fully turn ON, which is $\sim 15\times$ faster than the best case in prior art. It is also worth noting that this implementation of the proposed technique employs a low supply voltage of 1.0 V, which is one of the smallest among the compared prior art in Table II. Further speed-up can be achieved using a higher supply voltage as it allows a larger injection amplitude.

VII. CONCLUSION

This paper introduced a novel technique to kick-start high- Q oscillators, such as crystal and/or MEMS-based reference oscillators. The reduction in startup time is achieved through injecting energy into the resonator for a precise duration. A universal analysis for energy injection into high- Q resonators was presented and used to calculate the optimal injection duration essential to obtain a minimum startup time. We have also demonstrated that the proposed method ameliorates the sensitivity of the startup time to the matching between the injection and resonance frequencies over a range called the “TIFE”. This enables the use of integrated, temperature-compensated oscillators as the injection signal. The TIFE is analytically derived and proven that it is independent of the Q factor for high- Q resonators. Measurement results from a prototype IC, implemented in a 65-nm CMOS process, show that the proposed technique takes about 100–120 number of oscillation cycles in order to get started, which is by far the fastest startup time reported in the literature, to the best knowledge of the authors. The robustness of the proposed technique was verified by testing it across crystal devices from multiple manufacturers with different characteristics and frequencies.

APPENDIX

DERIVATION OF (3) AND (4)

Based on developing an analytic signal, the analysis in [38] states that the envelope of an arbitrary signal $i_m(t)$ is

$$i_{m,env}(t) = 2 \cdot \left| \frac{1}{2\pi} \int_{-\infty}^{+\infty} I_{m+}(j\omega) \cdot e^{j\omega t} d\omega \right| \quad (10)$$

where $I_{m+}(j\omega) = \mathcal{F}\{i_m(t)\}$ for $\omega > 0$. In case of the circuit shown in Fig. 6

$$i_{m,env}(t) = 2 \cdot \left| \frac{1}{2\pi} \int_{-\infty}^{+\infty} V_{inj+}(j\omega) \cdot H_+(j\omega) \cdot e^{j\omega t} d\omega \right| \quad (11)$$

where $I_{m+}(j\omega) = V_{inj+}(j\omega) \cdot H_+(j\omega)$ is used. Based on the fact that $H_+(j\omega)$ is a very high- Q filter centered at $\omega = \omega_m$

$$i_{m,env}(t) = |V_{inj+}(j\omega_m)| \cdot \left| \frac{1}{\pi} \int_{-\infty}^{+\infty} H_+(j\omega) \cdot e^{j\omega t} d\omega \right|. \quad (12)$$

Note that the second term in (12) is equal to the envelope of $h(t)$, hence

$$i_{m,env}(t) = |V_{inj+}(j\omega_m)| \cdot h_{env}(t) \quad (13)$$

$h_{env}(t = T_{inj})$ is a very slow-moving function over time that can be readily calculated as

$$h_{env}(t = T_{inj}) = \frac{1}{L_m} \cdot e^{-\frac{T_{inj}}{\tau}} \quad (14)$$

where $\tau = 2Q/\omega_m$ is the time constant of the circuit.

Now, let us consider the case of injecting a single tone, i.e., $v_S(t) = V_{inj} \cdot \cos(\omega_{inj}t)$. As should be noted in Fig. 1(b), the injection signal, in the frequency domain, is the convolution of the applied single tone with a sinc function. Hence

$$|V_{inj+}(j\omega)| = \frac{T_{inj} \cdot V_{inj}}{2} \cdot \left| \text{sinc} \left[\frac{T_{inj}}{2} (\omega_{inj} - \omega) \right] \right|. \quad (15)$$

The envelope of the motional current at the end of injection duration given by (4) is now readily proved by substituting (14) and (15) in (13).

ACKNOWLEDGMENT

The authors would like to thank R. Pallela and V. Paidi for their help with temperature testings.

REFERENCES

- [1] J. de Boeck, “IoT: The impact of Things,” in *Proc. Symp. VLSI Circuits (VLSI Circuits)*, Jun. 2015, pp. T82–T83.
- [2] K. Philips, “Ultra low power short range radios: Covering the last mile of the IoT,” in *Proc. 40th Eur. Solid-State Circuits Conf. (ESSCIRC)*, Sep. 2014, pp. 51–58.
- [3] C. C. Enz, A. El-Hoiydi, J. D. Decotignie, and V. Peiris, “WiseNET: An ultralow-power wireless sensor network solution,” *Computer*, vol. 37, no. 8, pp. 62–70, Aug. 2004.
- [4] Y.-H. Liu *et al.*, “A 3.7 mW-RX 4.4 mW-TX fully integrated Bluetooth low-energy/IEEE802.15.4/proprietary SoC with an ADPLL-based fast frequency offset compensation in 40 nm CMOS,” in *IEEE Int. Solid-State Circuits Conf. (ISSCC) Dig. Tech. Papers*, Feb. 2015, pp. 1–3.
- [5] B. Gosselin and M. Sawan, “Event-driven data and power management in high-density neural recording microsystems,” in *Proc. Joint IEEE North-East Workshop Circuits Syst. TAISA Conf.*, Jun./Jul. 2009, pp. 1–4.

- [6] Y. Chang, J. Leete, Z. Zhou, M. Vadipour, Y.-T. Chang, and H. Darabi, "A differential digitally controlled crystal oscillator with a 14-bit tuning resolution and sine wave outputs for cellular applications," *IEEE J. Solid-State Circuits*, vol. 47, no. 2, pp. 421–434, Feb. 2012.
- [7] D. Griffith, F. Dülger, G. Feygin, A. N. Mohieldin, and P. Vallur, "A 65 nm CMOS DCXO system for generating 38.4 MHz and a real time clock from a single crystal in 0.09 mm²," in *Proc. IEEE Radio Freq. Integr. Circuits Symp.*, May 2010, pp. 321–324.
- [8] R. van Langevelde, M. van Elzakker, D. van Goor, H. Termeer, J. Moss, and A. J. Davie, "An ultra-low-power 868/915 MHz RF transceiver for wireless sensor network applications," in *Proc. IEEE Radio Freq. Integr. Circuits Symp.*, Jun. 2009, pp. 113–116.
- [9] M.-D. Tsai, C.-W. Yeh, Y.-H. Cho, L.-W. Ke, P.-W. Chen, and G.-K. Dehng, "A temperature-compensated low-noise digitally-controlled crystal oscillator for multi-standard applications," in *Proc. IEEE Radio Freq. Integr. Circuits Symp.*, Jun. 2008, pp. 533–536.
- [10] S. Farahvash, C. Quek, and M. Mak, "A temperature-compensated digitally-controlled crystal Pierce oscillator for wireless applications," in *IEEE Int. Solid-State Circuits Conf. (ISSCC) Dig. Tech. Papers*, Feb. 2008, pp. 352–619.
- [11] J. Lin, "A low-phase-noise 0.004-ppm/step DCXO with guaranteed monotonicity in the 90-nm CMOS process," *IEEE J. Solid-State Circuits*, vol. 40, no. 12, pp. 2726–2734, Dec. 2005.
- [12] B. Razavi, *RF Microelectronics*, 2nd ed. Upper Saddle River, NJ, USA: Prentice-Hall, 2012.
- [13] A. Rusznayak, "Start-up time of CMOS oscillators," *IEEE Trans. Circuits Syst.*, vol. CAS-34, no. 3, pp. 259–268, Mar. 1987.
- [14] O. Yamashiro, "Initiation circuit in a crystal-controlled oscillator," U.S. Patent 4,039,973, Aug. 2, 1977. [Online]. Available: <https://www.google.mk/patents/US4039973>
- [15] M. Lin, "Fast wake-up crystal oscillating circuit," U.S. Patent 7,138,881, Nov. 21, 2006. [Online]. Available: <https://www.google.mk/patents/US7138881>
- [16] S. Iguchi, H. Fuketa, T. Sakurai, and M. Takamiya, "Variation-tolerant quick-start-up CMOS crystal oscillator with chirp injection and negative resistance booster," *IEEE J. Solid-State Circuits*, vol. 51, no. 2, pp. 496–508, Feb. 2016.
- [17] K. Jackoski, J. Simmons, and G. Schwieterman, "Method and apparatus for optimizing an oscillator start up time," U.S. Patent 5,844,448, Dec. 1, 1998. [Online]. Available: <https://www.google.mk/patents/US5844448>
- [18] S. M. Logan, "Oscillator with increased reliability start up," U.S. Patent 5,534,826, Jul. 9, 1996. [Online]. Available: <https://www.google.mk/patents/US5534826>
- [19] M. Ding et al., "A 95 μ W 24 MHz digitally controlled crystal oscillator for IoT applications with 36 nJ start-up energy and $>13\times$ start-up time reduction using a fully-autonomous dynamically-adjusted load," in *IEEE Int. Solid-State Circuits Conf. (ISSCC) Dig. Tech. Papers*, Feb. 2017, pp. 90–91.
- [20] S. A. Blanchard, "Quick start crystal oscillator circuit," in *Proc. 15th Biennial Univ. Government Ind. Microelectron. Symp.*, Jun. 2003, pp. 78–81.
- [21] Y.-I. Kwon, S.-G. Park, T.-J. Park, K.-S. Cho, and H.-Y. Lee, "An ultra low-power CMOS transceiver using various low-power techniques for LR-WPAN applications," *IEEE Trans. Circuits Syst. I, Reg. Papers*, vol. 59, no. 2, pp. 324–336, Feb. 2012.
- [22] Texas Instruments. (2015). *CC2650 SimpleLink Multistandard Wireless MCU, Datasheet*. [Online]. Available: <http://www.ti.com/lit/ds/symlink/cc2650.pdf>
- [23] D. Griffith, J. Murdock, and P. T. Røine, "A 24 MHz crystal oscillator with robust fast start-up using dithered injection," in *IEEE Int. Solid-State Circuits Conf. (ISSCC) Dig. Tech. Papers*, Jan./Feb. 2016, pp. 104–105.
- [24] H. Esmaeelzadeh and S. Pamarti, "A precisely-timed energy injection technique achieving 58/10/2 μ s start-up in 1.84/10/50 MHz crystal oscillators," in *Proc. IEEE Custom Integr. Circuits Conf.*, Apr./May 2017, pp. 1–4.
- [25] X. Zhang and A. B. Apsel, "A low-power, process-and- temperature-compensated ring oscillator with addition-based current source," *IEEE Trans. Circuits Syst. I, Reg. Papers*, vol. 58, no. 5, pp. 868–878, May 2011.
- [26] K. Sundaresan, P. E. Allen, and F. Ayazi, "Process and temperature compensation in a 7-MHz CMOS clock oscillator," *IEEE J. Solid-State Circuits*, vol. 41, no. 2, pp. 433–442, Feb. 2006.
- [27] N. Sadeghi, A. Sharif-Bakhtiar, and S. Mirabbasi, "A 0.007-mm² 108-ppm/ $^{\circ}$ C 1-MHz relaxation oscillator for high-temperature applications up to 180 $^{\circ}$ C in 0.13- μ m CMOS," *IEEE Trans. Circuits Syst. I, Reg. Papers*, vol. 60, no. 7, pp. 1692–1701, Jul. 2013.
- [28] J. Wang, W. L. Goh, X. Liu, and J. Zhou, "A 12.77-MHz 31 ppm/ $^{\circ}$ C on-chip RC relaxation oscillator with digital compensation technique," *IEEE Trans. Circuits Syst. I, Reg. Papers*, vol. 63, no. 11, pp. 1816–1824, Nov. 2016.
- [29] Y. Tokunaga, S. Sakiyama, A. Matsumoto, and S. Dosho, "An on-chip CMOS relaxation oscillator with voltage averaging feedback," *IEEE J. Solid-State Circuits*, vol. 45, no. 6, pp. 1150–1158, Jun. 2010.
- [30] Y.-K. Tsai and L.-H. Lu, "A 51.3-MHz 21.8-ppm/ $^{\circ}$ C CMOS relaxation oscillator with temperature compensation," *IEEE Trans. Circuits Syst. II, Exp. Briefs*, vol. 64, no. 5, pp. 490–494, May 2017.
- [31] E. A. Vittoz, M. G. R. Degrauwe, and S. Bitz, "High-performance crystal oscillator circuits: Theory and application," *IEEE J. Solid-State Circuits*, vol. SSC-23, no. 3, pp. 774–783, Jun. 1988.
- [32] J. Lu, S. Onishi, and Y. Tsuzuki, "A discussion on start-up time of crystal oscillators," (in Japanese), *IEEE J. Trans. Electron. Inf. Syst.*, vol. 111-C, no. 9, pp. 384–389, Sep. 1991.
- [33] E. Vittoz, *Low-Power Crystal and MEMS Oscillators*, 1st ed. Amsterdam, The Netherlands: Springer, 2010.
- [34] G. W. Pierce, "Piezoelectric crystal resonators and crystal oscillators applied to the precision calibration of wavemeters," *Proc. Amer. Acad. Arts Sci.*, vol. 59, no. 4, pp. 81–106, 1923. [Online]. Available: <http://www.jstor.org/stable/20026061>
- [35] G. W. Pierce, "Electrical system," U.S. Patent 2,133,642, Oct. 18, 1938. [Online]. Available: <https://www.google.mk/patents/US2133642>
- [36] A. M. Pappu, X. Zhang, A. V. Harrison, and A. B. Apsel, "Process-invariant current source design: Methodology and examples," *IEEE J. Solid-State Circuits*, vol. 42, no. 10, pp. 2293–2302, Oct. 2007.
- [37] S.-M. Kang and Y. Leblebici, *CMOS Digital Integrated Circuits Analysis & Design* (McGraw-Hill Series in Electrical and Computer Engineering). New York, NY, USA: McGraw-Hill, 2003. [Online]. Available: <https://books.google.com/books?id=1XyQ7RJ36cC>
- [38] M. Schwartz, W. R. Bennett, and S. Stein, *Communication Systems and Techniques*. New York, NY, USA: Wiley, 1995.



Hani Esmaeelzadeh (S'14) received the B.S. degree in electrical engineering from the K.N. Toosi University of Technology, Tehran, Iran, in 2011, and the M.S. degree in electrical engineering from the Sharif University of Technology, Tehran, in 2013. He is currently pursuing the Ph.D. degree in electrical engineering with the University of California at Los Angeles (UCLA), Los Angeles, CA, USA.

From 2016 to 2017, he held an internship position at Qualcomm Technologies, Inc., San Diego, CA, USA, where he was involved in RFIC design for cellular applications. His current research interests include analog, mixed-signal, and RF circuit design.

Mr. Esmaeelzadeh was a recipient of the UCLA Graduate Division Fellowship in 2014 and the Broadcom Foundation Fellowship from 2016 to 2017. He is also a recipient of the Broadcom Foundation Fellowship from 2017 to 2018.



Sudhakar Pamarti (S'98–M'03) received the B.Tech. degree in electronics and electrical communication engineering from IIT Kharagpur, Kharagpur, India, in 1995, and the M.S. and Ph.D. degrees in electrical engineering from the University of California at San Diego, San Diego, CA, USA, in 1999 and 2003, respectively.

From 1995 to 1997, he was with Hughes Software Systems, New Delhi, India, where he was involved in the development of embedded software and firmware for a wireless communication system.

From 2003 to 2005, he was with Rambus Inc., Sunnyvale, CA, USA, where he was involved in developing high-speed I/O circuits. He is currently a Professor of electrical engineering with the University of California at Los Angeles, Los Angeles, CA, USA. His current interests include integrated circuit design with a special focus on developing algorithmic techniques to overcome circuit impairments.

Dr. Pamarti was a recipient of the National Science Foundation's CAREER Award. He currently serves on the Technical Program Committees of the IEEE Custom Integrated Circuits Conference and the IEEE International Solid-State Circuits Conference, and as an Associate Editor for the IEEE TRANSACTIONS ON CIRCUITS AND SYSTEMS PART I-REGULAR PAPERS.